

PAPER

## Graphene surface plasmons mediated thermal radiation

To cite this article: Jiayu Li *et al* 2018 *J. Opt.* **20** 024011

View the [article online](#) for updates and enhancements.



**IOP | ebooks™**

Bringing together innovative digital publishing with leading authors from the global scientific community.

Start exploring the collection—download the first chapter of every title for free.

# Graphene surface plasmons mediated thermal radiation

Jiayu Li, Baoan Liu and Sheng Shen<sup>1</sup> 

Department of Mechanical Engineering, Carnegie Mellon University, Pittsburgh, PA, 15213, United States of America

E-mail: [sshen1@cmu.edu](mailto:sshen1@cmu.edu)

Received 30 August 2017, revised 11 December 2017

Accepted for publication 14 December 2017

Published 16 January 2018



CrossMark

## Abstract

A graphene nanostructure can simultaneously serve as a plasmonic optical resonator and a thermal emitter when thermally heated up. The unique electronic and optical properties of graphene have rendered tremendous potential in the active manipulation of light and the microscopic energy transport in nanostructures. Here we show that the thermally pumped surface plasmonic modes along graphene nanoribbons could dramatically modulate their thermal emission spectra in both near- and far-fields. Based on the fluctuating surface current method implemented by the resistive boundary method, we directly calculate the thermal emission spectrum from single graphene ribbons and vertically paired graphene ribbons. Furthermore, we demonstrate that both the near- and far-field thermal emission from graphene nanostructures can be optimized by tuning the chemical potential of doped graphene. The general guideline to maximize the thermal emission is illustrated by the our recently developed theory on resonant thermal emitters modulated by quasi-normal modes.

Keywords: graphene surface plasmonics, thermal radiation, fluctuating surface current method, 2D resistive boundary

(Some figures may appear in colour only in the online journal)

## 1. Introduction

A graphene nanostructure can simultaneously function as a plasmonic optical resonator and a thermal emitter [1, 2]. As the plasmonic optical resonator, graphene nanostructures can support strongly confined and highly tunable surface plasmons [3, 4]. The strong confinement of electromagnetic waves around graphene nanostructures enables the manipulation and control of the light in the scale that is almost two orders of magnitude smaller than the light wavelength in the free space [2]. In particular, the graphene plasmons excited in the mid-infrared range exhibit less loss than those in conventional noble metals [5]. By changing the chemical potential of graphene through gating or doping, the optoelectronic properties of graphene can be actively tuned [6–8],

resulting in dramatic change in the plasmonic spectrum. As the thermal emitter, graphene nanostructures are the key for designing tunable thermal emitters and absorbers in the Terahertz range [1, 9, 10]. In addition, the extremely small thermal mass of graphene in conjunction with the strong interaction with light opens up an avenue of graphene based thermal plasmonics, invoking the applications from infrared emission control [11] to information processing [12] and energy harvesting [13]. Graphene based nanostructures, such as nano-ribbons, rings, and disks, could become the building blocks for many promising thermal infrared devices [2]. In this work, we perform direct numerical calculations on the thermal emission spectrum of single graphene ribbons and vertically-paired graphene ribbons. Using the fluctuating surface current (FSC) method [14] implemented by the resistive boundary formulation [12], both far field and near field thermal emission of graphene nanoribbon structures are investigated. Combining our recently developed Quasi-normal mode (QNM) theory on resonant thermal emitters

<sup>1</sup> This article belongs to the special issue: [Emerging Leaders](#), which features invited work from the best early-career researchers working within the scope of the *Journal of Optics*. Professor Dr Sheng Shen was selected by the Editorial Board of the *Journal of Optics* as an Emerging Leader.

[15, 16], the relationship between thermal emission and graphene chemical potential is analyzed based on fractional mode loss calculations.

As more and more research efforts are being drawn to the field of graphene plasmonics and its relevant applications, efficiently solving the Maxwell equation in graphene becomes imperative. In most cases, there are no analytical solutions to the Maxwell equation except some canonical problems. Among the mainstream numerical methods for solving the Maxwell equation, namely finite-difference-time-domain (FDTD) method, finite element method (FEM) and method of moment (MoM), no specific algorithms have been developed for the case of two-dimensional (2D) materials like graphene. Until recently, a few approaches are put forward to tackle this problem. For the FDTD method [17, 18], the graphene layer can be approximated as a thin film with a finite thickness around 1 nm occupying several mesh steps, where the volumetric conductivity is converted from the surface conductivity of graphene and the background permittivity. Another alternate approach in FDTD is to treat graphene as a thin layer occupying only a fraction of the Yee cell with a specially designed perfect match layer. The most efficient way to deal with graphene using FDTD compared to the previous two methods is to model it as a resistive zero-thickness sheet over which the fields satisfy surface boundary conduction induced by surface conductivity [19, 20]. For the FEM method, similar approaches [21, 22] have been taken to model the graphene as a thin film layer using conversion between volumetric and surface conductivity. For the MoM, it is known for its high efficiency solving electrically large objects, and is widely used in solving radiation and scattering problems. Analytical expression of the dyadic Green's function has been derived for graphene in the MoM [23, 24]. Integral equations based on surface-impedance boundary conditions are formulated to analyze plan wave scattering and absorption by graphene gratings [25]. The MoM for graphene nanoribbons are also developed [26]. However, the efficiency and accuracy of the electromagnetic response simulation from graphene remain a problem for the current numerical methods.

## 2. Method

### 2.1. FSC method for directly calculating the thermal radiation from graphene

Combining the fluctuation dissipation theorem (FDT) with the boundary element method (BEM), the FSC method has been proved to be a highly-efficient computational tool for calculating the thermal radiation from arbitrary geometries [12, 14, 27, 28]. When simulating the electromagnetic response of a structure due to thermally induced fluctuating currents, only the surface boundary mesh is needed, which leads to superior computational efficiency. The key of the FSC method is to solve the surface integral equation (SIE) under the framework of Galerkin method in the standard matrix solution like LU-decomposition. Equivalent surface

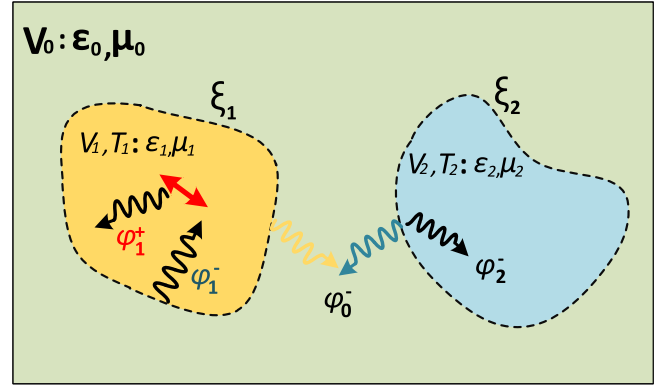


**Figure 1.** Two different bulk materials of random geometries in the vacuum space at temperatures  $T_1$  and  $T_2$ .

currents  $\xi_i$  on the surface boundary between various spatial regions serve as the source to the stochastic Maxwell's equation where the homogenous Dyadic Green's function  $\Gamma_i$  is involved in calculating the real electromagnetic response  $(E, H)^T$ . To further illustrate the formalism of the FSC method, Huygens's equivalence principle is thereby introduced as it is the foundation for the BEM in such electromagnetic simulations [29, 30].

For two bulk materials with permittivity and permeability  $(\epsilon_1, \mu_1)$  and  $(\epsilon_2, \mu_2)$  placed in the free space, the SIE has already been described in detail by [14], which gives the following formula

$$\begin{aligned} \hat{n}_1 \times [(\Gamma_0 + \Gamma_1) * \xi_1 + \Gamma_0 * \xi_2] &= \hat{n}_1 \times [\psi_1^+ - \psi_0^+] \\ \hat{n}_2 \times [(\Gamma_0 + \Gamma_2) * \xi_2 + \Gamma_0 * \xi_1] &= \hat{n}_2 \times [\psi_2^+ - \psi_0^+]. \end{aligned} \quad (1.1)$$

$\psi_i^+$  is the incident electromagnetic field that comes from the bulk material without scattering. In the scenario of thermal radiation, the source of field  $\psi_i^+$  originates from the thermally excited current density  $J_i(r, \omega)$ .  $\hat{n}_i$  is the outward normal unit vector at the boundary of the bulk material  $\partial V_i$ . The schematic is shown in figure 1. Using the Galerkin method to discretize the SIE, the equivalent surface currents  $\xi_i$  can be expanded by a set of  $N$  basis surface functions  $\beta_i^n(r)$  on the boundary  $\partial V_i$  with coefficient  $\{x_i^n\}$ , that is  $\xi_i(r) = \sum_n x_i^n \beta_i^n(r)$ . The discretized SIE equation is given as the following matrix form

$$\begin{bmatrix} \langle \beta_1 | (\Gamma_0 + \Gamma_1) * \beta_1 \rangle & \langle \beta_1 | \Gamma_0 * \beta_2 \rangle \\ \langle \beta_2 | \Gamma_0 * \beta_1 \rangle & \langle \beta_2 | (\Gamma_0 + \Gamma_2) * \beta_2 \rangle \end{bmatrix} \begin{bmatrix} \langle \xi^1 | \beta_1 \rangle \\ \langle \xi^1 | \beta_2 \rangle \end{bmatrix} = \begin{bmatrix} \langle \beta_1 | \psi_1^+ - \psi_0^+ \rangle \\ \langle \beta_2 | \psi_2^+ - \psi_0^+ \rangle \end{bmatrix}. \quad (1.2)$$

The matrix can be further expanded into three BEM matrix as  $M = M_0 + M_1 + M_2$ , where

$$\begin{aligned} M_0 &= \begin{bmatrix} \langle \beta_1 | \Gamma_0 * \beta_1 \rangle & \langle \beta_1 | \Gamma_0 * \beta_2 \rangle \\ \langle \beta_2 | \Gamma_0 * \beta_1 \rangle & \langle \beta_2 | \Gamma_0 * \beta_2 \rangle \end{bmatrix}, \\ M_1 &= \begin{bmatrix} \langle \beta_1 | \Gamma_1 * \beta_1 \rangle & 0 \\ 0 & 0 \end{bmatrix}, \\ M_2 &= \begin{bmatrix} 0 & 0 \\ 0 & \langle \beta_2 | \Gamma_2 * \beta_2 \rangle \end{bmatrix}. \end{aligned} \quad (1.3)$$

Here, the matrix  $M_0$  represents the multi-body interactions via the waves in the free space  $V_0$ , and the matrices  $M_1$  and  $M_2$  represent self-interaction via waves inside the regions  $V_1$  and  $V_2$  respectively.

For the case that  $V_1$  at the temperature of  $T_1$  and  $V_2$  at the temperature of  $T_2$  ( $T_1 > T_2$ ), the FSC method describes the thermal radiative energy transfer from  $V_1$  to  $V_2$  as

$$\Psi = \int_0^\infty d\omega [\Theta(\omega, T_1) - \Theta(\omega, T_2)] \phi_{1 \rightarrow 2}(\omega), \quad (1.4)$$

where  $\Theta(\omega, T) = \hbar\omega / (\exp(\hbar\omega/k_B T) - 1)$  and the spectral energy flux  $\phi_{1 \rightarrow 2}(\omega)$  can be calculated from the BEM matrix  $M$  and self-interaction matrix  $M_1$  and  $M_2$  as

$$\phi_{1 \rightarrow 2}(\omega) = \frac{2}{\pi} \text{Tr}[\text{sym}[M_1]M^{-1} * \text{sym}[M_2]M^{-1} *]. \quad (1.5)$$

In equation (1.5),  $\text{Tr}[\cdot]$  denotes the trace of the matrix,  $\text{sym}[A] = \frac{1}{2}(A + A^*)$  and  $M^{-1}$  indicates the inverse matrix of  $M$ . In addition, the thermal emission from  $V_1$  to the far-field can be obtained as

$$\phi_{1 \rightarrow 0}(\omega) = \frac{2}{\pi} \text{Tr}[\text{sym}[M_1]M^{-1} * \text{sym}[M_0]M^{-1} *]. \quad (1.6)$$

## 2.2. FSC method for 2D materials

Although the FSC method works well for bulk materials with high efficiency, it encounters much difficulty when dealing with 2D materials like graphene. Two factors are attributed to the failure of the conventional FSC method. First, the sub-nanometer scale of the thickness of 2D materials makes it very hard to mesh the structure when one evaluates it as a thin film [2, 31], especially for the FEM and FDTD methods. Second, even though the thin-film approximation can still be applied, the BEM simulation can become very inefficient in assembling the self-interaction matrix of the thin-film due to its very large effective permittivity resulting from the volume conductivity. For the first factor, the computation and meshing constraints have been greatly released by the advanced development of high-performance computers. For the second factor, the large effective permittivity  $\varepsilon = \varepsilon_r + i \frac{\sigma_s}{\varepsilon_0 \omega \Delta}$  reduces the BEM simulation's efficiency in the evaluation of the homogeneous Green's function  $G_i(r, r') = [I + \varepsilon_i \mu_i \omega^2] \frac{e^{i\varepsilon_i \mu_i \omega^2 |r-r'|}}{4\pi |r-r'|}$ , and leads to a large difference between the diagonal and off-diagonal elements of the self-interaction matrix. Here, we exactly model it as a 2D resistive boundary with an in-plane conductivity  $\sigma_s(\omega)$  [32]. Such the in-plane ( $x$ - $y$  plane) conductivity  $\sigma_s(\omega)$  is related to the volumetric conductivity as  $\delta(z)\sigma_s = \sigma_v$  for the 2D material located at  $z = 0$ . It thus leads to  $j_{x,y} = \sigma_s \delta(z) E_{x,y}$ .

The main task of this formalism is to search for a new SIE for the 2D resistive boundary. We first start with applying Huygens's equivalence principle to this 2D resistive boundary  $S$  as shown in figure 2(a). An auxiliary boundary  $S'$  is added to connect the ends of  $S$  through the vacuum, which then divides the vacuum space into two regions  $V_0$  and  $V_1$ . Now the fictitious surface current as described in the previous section

can be put on the newly-created boundary to serve as equivalent current sources. It should be noted here that the boundary condition at the surface  $S$  now becomes

$$\begin{aligned} \widehat{n}_0 \times (E_0 - E_1) &= 0 \\ \widehat{n}_0 \times (H_0 - H_1) &= \sigma_s E_0 + J_{\text{ext}}, \end{aligned} \quad (1.7)$$

where  $[E_0, H_0]$  is the field at the top of the surface, and  $[E_1, H_1]$  is the field at the bottom of the surface.  $\sigma_s E_0$  indicates the induced currents on the resistive boundary due to the electric field.  $J_{\text{ext}}$  denotes the thermally induced surface current sources in  $S$  that is well described by the FDT theorem [33].

The fictitious surface currents in region  $V_0$  can be defined as  $\xi_0 = \begin{pmatrix} J_0 \\ K_0 \end{pmatrix} = \begin{pmatrix} \widehat{n}_0 \times H_0 \\ -\widehat{n}_0 \times E_0 \end{pmatrix}$  on  $S$ , and  $\xi'_0 = \begin{pmatrix} J'_0 \\ K'_0 \end{pmatrix} = \begin{pmatrix} \widehat{n}_0 \times H_0 \\ -\widehat{n}_0 \times E_0 \end{pmatrix}$  on  $S'$ . For the region  $V_1$ , they are defined as  $\xi_1 = \begin{pmatrix} J_1 \\ K_1 \end{pmatrix} = \begin{pmatrix} \widehat{n}_1 \times H_1 \\ -\widehat{n}_1 \times E_1 \end{pmatrix}$  on  $S$  and  $\xi'_1 = \begin{pmatrix} J'_1 \\ K'_1 \end{pmatrix} = \begin{pmatrix} \widehat{n}_1 \times H_1 \\ -\widehat{n}_1 \times E_1 \end{pmatrix}$  on  $S'$ . Considering boundary conditions on the auxiliary surface  $S'$ , it has  $\xi'_0 = -\xi'_1$ . Applying Huygens's equivalence principle, the fields in different regions can be expressed as

$$\begin{aligned} \psi_0(r) &= \begin{pmatrix} E_0(r) \\ H_0(r) \end{pmatrix} = \frac{\psi_0^+(r) + \Gamma_0 * (\xi_0 + \xi'_0)}{\theta(r)} \\ \psi_1(r) &= \begin{pmatrix} E_1(r) \\ H_1(r) \end{pmatrix} = \frac{\Gamma_0 * \xi_0 - \Gamma_0 * \xi'_0}{\theta(r)}, \end{aligned} \quad (1.8)$$

where again we assume that there is no active current source in region  $V_0$  and  $\theta(r)$  is defined the same as stated in the previous section. Applying boundary conditions mentioned before on both boundaries  $S$  and  $S'$ , the new SIE of the 2D resistive boundary can be derived as

$$\widehat{n}_0 \times \left[ \Gamma_0^{EE} * J_S - \frac{1}{\sigma_s} J_S \right] = \widehat{n}_0 \times \left[ -\frac{J_{\text{ext}}}{\sigma_s} - E_0^+ \right]. \quad (1.9)$$

In the new formalism for the SIE,  $J_S = J_0 + J_1$  represents the total fictitious surface current on the boundary  $S$ .  $\Gamma_0^{EE}$  stands for the electric field response part of the Dyadic Green's tensor within an infinite region  $V_0$ . Compared with the SIE derived for bulk materials in equations (1.1) and (1.9), only the electric current  $J_S$  is required for the 2D resistive boundaries. Again, the new SIE can be discretized by the Galerkin method with a set of basis surface functions defined on the boundary  $S$  as

$$\begin{aligned} & \left[ \left\langle \beta \left| \begin{bmatrix} \Gamma_0^{EE} & 0 \\ 0 & 0 \end{bmatrix} * \beta \right\rangle + \begin{bmatrix} -1/\sigma_s & 0 \\ 0 & 0 \end{bmatrix} \langle \beta | \beta \rangle \right] [\langle \xi_S | \beta \rangle] \\ & = \left[ \left\langle \beta \left| \begin{pmatrix} -J_{\text{ext}}/\sigma_s \\ 0 \end{pmatrix} - \psi_0^+ \right\rangle \right]. \end{aligned} \quad (1.10)$$

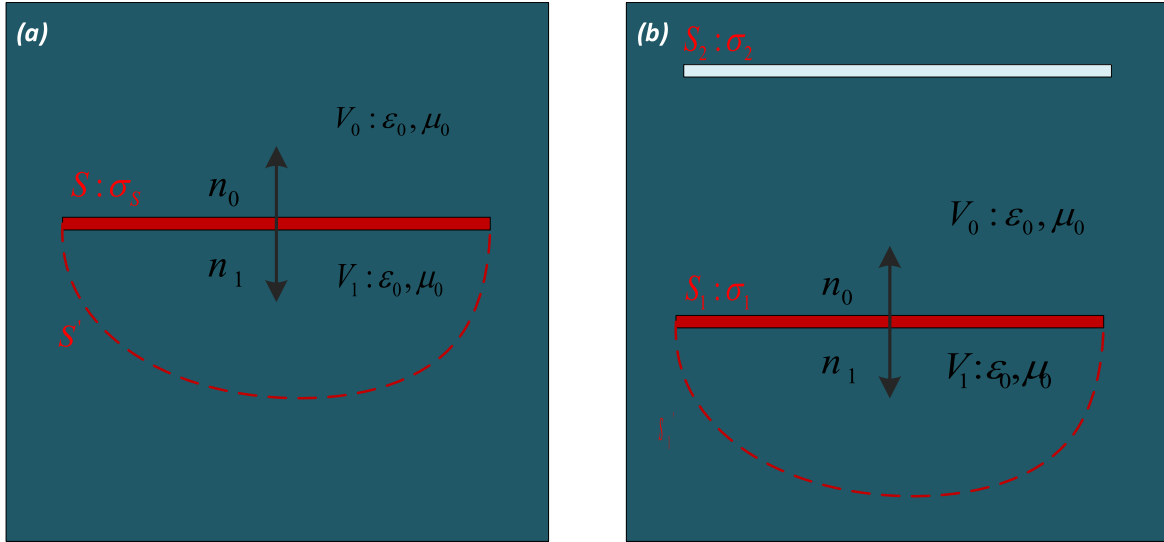


**Figure 2.** Huygen's equivalent principle for (a) single 2D resistive boundary and (b) two 2D resistive boundaries, the dashed red line denotes the auxiliary boundary,  $\sigma_s$ ,  $\sigma_1$  and  $\sigma_2$  denote the surface conductivity in the resistive boundaries.  $\hat{n}_0$  and  $\hat{n}_1$  are the normal unit vector at the top and bottom surface of the resistive boundary.

For the case of two 2D resistive boundaries as shown in figure 2(b), similar procedure can be taken to obtain the corresponding SIE. Consider the resistive boundary  $S_1$  as the emitter and  $S_2$  as the absorber suspended in the free space  $V_0$ . Assume fictitious surface currents  $\xi_1 = \begin{pmatrix} J_1 \\ 0 \end{pmatrix}$  on  $S_1$  and  $\xi_2 = \begin{pmatrix} J_2 \\ 0 \end{pmatrix}$  on  $S_2$ . The resulted BEM equation with the form of  $Mx = s$  can be derived as

$$[M_0 + M_1 + M_2] \begin{bmatrix} \langle \xi_1 | \beta_1 \rangle \\ \langle \xi_2 | \beta_2 \rangle \end{bmatrix} = \begin{bmatrix} \left\langle \beta_{11} \left( \begin{matrix} -J_{ext}/\sigma_1 \\ 0 \end{matrix} \right) \right\rangle \\ 0 \end{bmatrix}, \quad (1.11)$$

where  $\beta_1$  and  $\beta_2$  are the basis function for  $S_1$  and  $S_2$  respectively.  $J_{ext}$  indicates the thermally induced random currents inside  $S_1$ . The multi-body interaction matrix  $M_0$  and the self-interaction matrices  $M_1$  and  $M_2$  are expressed as

$$M_0 = \begin{bmatrix} \left\langle \beta_{11} \begin{bmatrix} \Gamma_0^{EE} & 0 \\ 0 & 0 \end{bmatrix} * \beta_1 \right\rangle & \left\langle \beta_{11} \begin{bmatrix} \Gamma_0^{EE} & 0 \\ 0 & 0 \end{bmatrix} * \beta_2 \right\rangle \\ \left\langle \beta_{21} \begin{bmatrix} \Gamma_0^{EE} & 0 \\ 0 & 0 \end{bmatrix} * \beta_1 \right\rangle & \left\langle \beta_{21} \begin{bmatrix} \Gamma_0^{EE} & 0 \\ 0 & 0 \end{bmatrix} * \beta_2 \right\rangle \end{bmatrix},$$

$$M_1 = \begin{bmatrix} \left( \frac{-1}{\sigma_1} \right) I_0^3 \langle \beta_1 | \beta_1 \rangle & 0 \\ 0 & 0 \end{bmatrix},$$

$$M_2 = \begin{bmatrix} 0 & 0 \\ 0 & \left( \frac{-1}{\sigma_2} \right) I_0^3 \langle \beta_2 | \beta_2 \rangle \end{bmatrix} \quad (1.12)$$

with  $I_0^3$  denoting

$$I_0^3 = \begin{bmatrix} -\frac{1}{\sigma_s} & & & & & \\ & -\frac{1}{\sigma_s} & & & & \\ & & -\frac{1}{\sigma_s} & & & \\ & & & 0 & & \\ & & & & 0 & \\ & & & & & 0 \end{bmatrix}. \quad (1.13)$$

Finally, the radiative energy transfer between two 2D resistive boundaries is obtained as

$$\phi_{1 \rightarrow 2}(\omega) = \frac{2}{\pi} \text{Tr}[\text{sym}[M_1]M^{-1} * \text{sym}[M_2]M^{-1} *], \quad (1.14)$$

which is equal to the energy absorbed by  $S_2$ . It should be noted that equation (1.14) has the similar form as equation (1.5) except the expression of the self-interaction matrices  $M_1$  and  $M_2$ . In the BEM, the basis function  $\{\beta_n\}$  is usually chosen as the piecewise-polynomial element functions. Specially, we adopt the Rao–Wilton–Glisson basis functions for the general three-dimensional structures, and 2D roof-top basis functions for the structures invariant in one direction.

### 3. Results and discussion

#### 3.1. Far-field thermal radiation

We first investigate the thermal radiation emitted from single graphene nanoribbon placed in vacuum, and then move on to the vertically paired graphene nanoribbons. Figure 3 shows

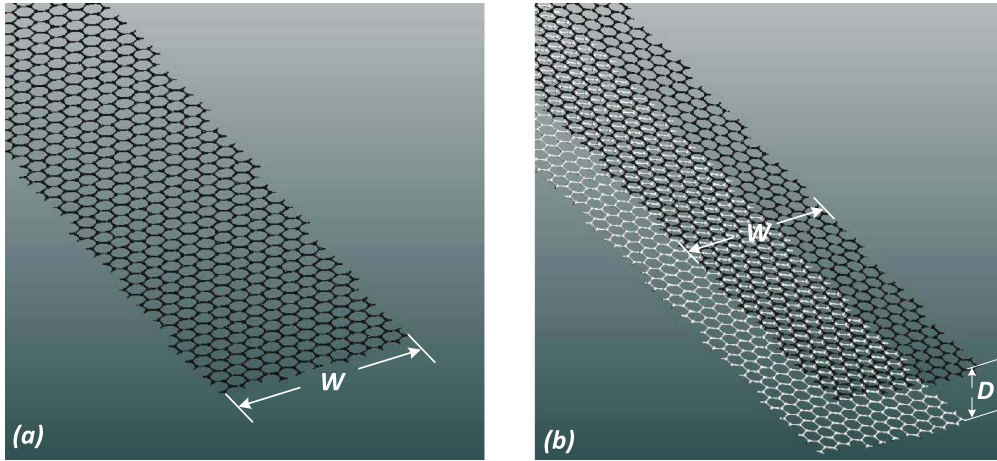


**Figure 3.** Schematics of (a) single graphene nanoribbon with width  $W$ , (b) and vertically paired graphene nanoribbons with width  $W$  and gap distance  $D$ .

the schematics of them. The far-field radiative heat flux is calculated by the FSC method implemented by the resistive boundary method. The surface electrical conductivity response function  $\sigma(\omega, k_{\parallel}, E_F)$  is described by intra-band and inter-band transitions, where  $k_{\parallel}$  is the in-plane wavevector and  $E_F$  is the Fermi level of the graphene nanoribbon. In our calculation, we adopt the surface conductivity formulation derived from random phase approximation method [34] in the limit of  $k_{\perp} \rightarrow 0$ .

$$\sigma(\omega) = \frac{e^2 E_F}{\pi \hbar^2} \frac{i}{\omega + i\tau^{-1}} + \frac{e^2}{4\hbar} [\theta(\hbar\omega - 2E_F) + \frac{i}{\pi} \log \left| \frac{\hbar\omega - 2E_F}{\hbar\omega + 2E_F} \right|]. \quad (1.15)$$

The first and second terms of this equation represent the intra-band and the inter-band contributions, respectively. In our calculation, the intra-band contribution dominates since the energy of the thermal excited photons are smaller than the Fermi level. The width of the graphene nanoribbon is set to be 100 nm, and its Fermi level ranges from 0.2 to 3.5 eV. The relaxation time of electrons in graphene nanoribbon  $\tau$  is set to be  $2 \times 10^{-13}$  s. The electron relaxation time is estimated from the measurement of the impurity dc mobility [35], and this value is conservative compared to the recent experimental measurements [36]. Here, the neglect of the spatial dispersion is justified by calculating the phase velocity of graphene surface plasmon which turns out to be almost one order of magnitude larger than the Fermi velocity.

The linear dispersion relation of the electrical states in graphene, especially around the Dirac point, leads to great tunability of its optoelectronic properties. The excess of the electrons or holes in doped graphene can support collective surface plasmons. When thermally heated up, various plasmonic modes along the nanoribbon direction are spontaneously excited [12, 37, 38], such as the edge graphene surface plasmon (EGSP) modes [39]. Since such a single graphene nanoribbon simultaneously performs as a thermal emitter and a plasmonic optical resonator, the far-field thermal radiation can be narrow-band and modulated by its resonant

modes. As illustrated in our previous work [15, 16], the general principle of designing optical resonator thermal emitter with perfect or maximized emission in both near- and far-fields is to match the resistive and radiative losses. The resistive losses include the energy dissipation in the emitter  $D_E = \int_{V_E} dr^3 \frac{1}{2} \sigma_E(\text{Re}[\omega]) |E(r)|^2$  and in the absorber  $D_A = \int_{V_A} dr^3 \frac{1}{2} \sigma_A(\text{Re}[\omega]) |E(r)|^2$ , where  $V_E$ ,  $V_A$  and  $\sigma_E$ ,  $\sigma_A$  are the volume and the electrical conductivity of the emitter and absorber respectively. The radiative loss is expressed as  $D_{\infty} = \int_{\partial V} dr^2 \frac{1}{2} \text{Re}[E(r) \times H^{\dagger}(r)]$  and has the form of mode energy loss due to far-field radiation, where  $\dagger$  denotes the conjugate-transpose and  $\partial V$  represents the enclosed surface around the system. Following the illustration of the mode losses, the fractional mode loss of the emitter, the near-field absorber and the far field can be defined as  $\eta_E = \frac{D_E}{D_E + D_A + D_{\infty}} F$ ,  $\eta_A = \frac{D_A}{D_E + D_A + D_{\infty}} F$  and  $\eta_{\infty} = P - \eta_E - \eta_A$ . The  $F$  and  $P$  are the imperfection factor and  $F$  is approximated to be 1 due to the quasi-static condition in the graphene nanoribbon structure. The maxima of the near-field thermal emission  $\phi_A$  and far-field thermal emission  $\phi_{\infty}$  are equal to  $P^2$ , when  $\eta_E = \eta_A = \frac{P}{2}$  and  $\eta_{\infty} = 0$  for near-field cases, and  $\eta_E = \eta_{\infty} = \frac{P}{2}$ ,  $\eta_A = 0$  for far-field cases.

In this case, the excitation of the second EGSP mode in graphene nanoribbons plays a major role as the predominant mode for the far-field thermal radiation. As shown in figure 4, the white crosses represent the first EGSP mode and the white dotted line is the second EGSP mode. The white circles represent the light line in the free space. The majority of the first EGSP mode lies in the evanescent wave region such that the first mode does not make the contribution. Part of the second EGSP mode is within the propagating region and makes the major contribution to the far-field thermal radiation. Particularly, the strong peak that exists in the far-field thermal emission spectrum for each Fermi level arises from the excitation of the localized EGSP mode. The wavelength of the localized EGSP is the half of the nanoribbon width and the EGSP travels forward and backward along the width direction.

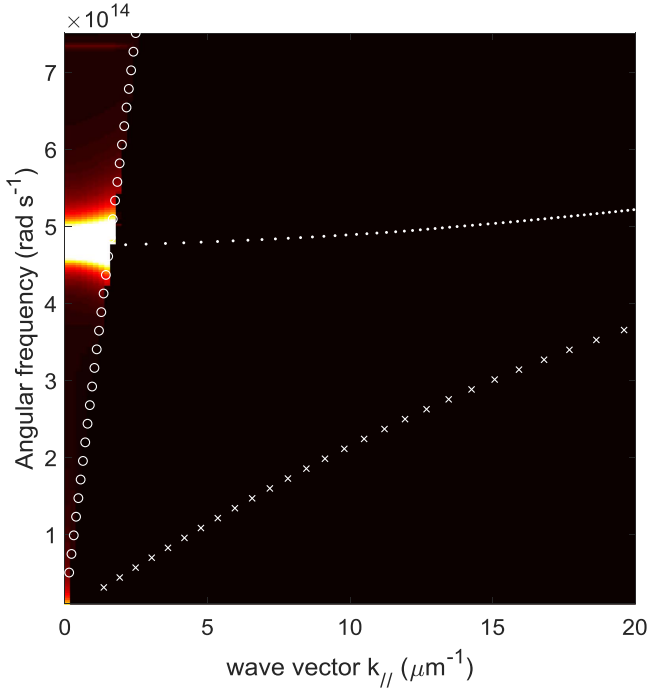


**Figure 4.** Contribution from each photon mode  $(\omega, k_{//})$  for the single free-standing graphene nanoribbon with Fermi level of 1.5 eV. The white circles represent the light line in the free space. The white crosses represent the first EGSP mode. The white dotted line represents the second EGSP mode.

Normalized real part of the electric field amplitude for this mode along the ribbon width direction is plotted in figure 5(c). In order to maximize the far field thermal radiation from the single graphene nanoribbon, the resistive mode loss  $\eta_E$  and radiative mode loss  $\eta_\infty$  should be balanced. In doped graphene, the resistive mode loss mainly results from the scattering of the electron collective oscillation with the EGSP modes. It should be noted that the intra-band Drude-like term dominates the graphene surface conductivity in our considered frequency range ( $2 \times 10^{14}$ – $6 \times 10^{14}$  rad s<sup>-1</sup>). With the increasing doping level, the number of charged carriers involved in the plasmonic oscillation increases, which leads to the increase of the resistive loss  $\eta_E$  in the graphene nanoribbon [40]. As a result, the resistive mode loss  $\eta_E$  within the graphene nanoribbon could be actively tuned by the doping level. Furthermore, the electron relaxation time in our case is fixed to be  $2 \times 10^{-13}$  s and the total loss of the electron scattering process (electron–photon scattering, electron–phonon scattering and electron–electron scattering) is also fixed. In this case, the increasing doping level leads to the decrease of the carrier mobility and the increase of the effective plasmon mode index, and in turn suppresses the radiative decay of the plasmon excitation. We estimate the radiative loss in the graphene nanoribbon by evaluating the total dipole moment induced by the localized EGSP mode. Here, we estimate the total dipole moment under quasi-single electron approximation as  $\vec{\mu}(\omega, E_F) \sim \zeta \frac{ne |E| \mu_c}{\omega} = \zeta \frac{ne^2 V_F^2 \tau}{\omega E_F} |E|$  with a screening factor  $\zeta$ . The Fermi energy is tuned by electrical gating.  $\tau$  is the relaxation time of electrons in graphene,  $n$  is the electron

concentration density,  $\mu_c$  is the mobility of electrons and  $|E|$  is the electrical field intensity along the graphene width direction. The resistive and radiative losses of the monopole plasmons corresponding to different doping levels are calculated plotted in figure 5 based on the formulation derived in [15]. As shown in figure 5(a), the resistive loss  $\eta_E$  is represented by the red line while the radiative loss is plotted by the blue line. The reduced radiative heat flux  $2\pi\phi_\infty/\Theta$  into the far-field is plotted in figure 5(b) with the upper limit of  $P^2$ . The imperfection factor  $P$  is due to the non-Hermitian factor in graphene nanoribbon, as plotted with the black line in the figure 5(a). At the doping level around 2.5 eV, the resistive loss  $\eta_E$  and radiative loss  $\eta_\infty$  approximately match with each other, giving rise to the maximization of the radiative heat flux into the far-field. Beyond this point, the resistive loss begins to outweigh the radiative loss, leading to the decrease of the radiative heat flux in the far field. The detailed radiative heat flux spectra are illustrated in figure 5(b). While the tuning range of the graphene Fermi level is up to 3.5 eV which may be unrealistic, it should be noted that the main objective of this work is to demonstrate that the optimized thermal emission is achievable by tuning and then matching the corresponding radiative and resistive losses. Other than tuning doping level, changing the geometry of the graphene nanoribbon can potentially optimize the far-field radiative heat flux. However, it turns out that the width of the graphene nanoribbon has very limited influence on the radiative heat flux because elongating the width increases both the radiative loss [41, 42] and the resistive dissipation. As a consequence, the ratio of the  $\eta_E$  and  $\eta_\infty$  remains almost unchanged as shown in figure 6(a), where the Fermi level and the electron scattering time of the investigated cases are fixed to be 0.5 eV and  $2 \times 10^{-13}$  s respectively. Although an optimized radiative heat flux is achieved around the width of 150 nm in figure 6(b), the tunability is still far smaller than that by changing the chemical potential.

### 3.2. Near-field thermal radiation

While the far-field radiative heat flux is bound by the upper limit defined by  $\frac{\Theta}{2\pi}$ , the radiative heat flux in the near-field can significantly exceed it [43]. Photon tunneling effect gradually takes the major role as the distance between a thermal emitter and an absorber decreases, and makes great contribution to the radiative energy transfer when the distance is smaller than the thermal wavelength defined by Wien’s law. For the case of the vertically paired graphene nanoribbons, the gap distance between two ribbons is set to be 100 nm and the width of the two ribbons is 100 nm. The electron relaxation time is still  $2 \times 10^{-13}$  s. As the two graphene nanoribbons are placed at a distance that is smaller than the wavelength of propagating surface plasmons, the interaction between the two strongly confined fields around the graphene ribbons leads to the hybridization of plasmon modes [44]. At large separations, the mode hybridization and splitting occur. For our case, the two separate EGSP modes excited around two graphene nanoribbons are combined to form two types of hybridized states, namely symmetric bonding and anti-symmetric bonding of two EGSP modes. Decreasing the

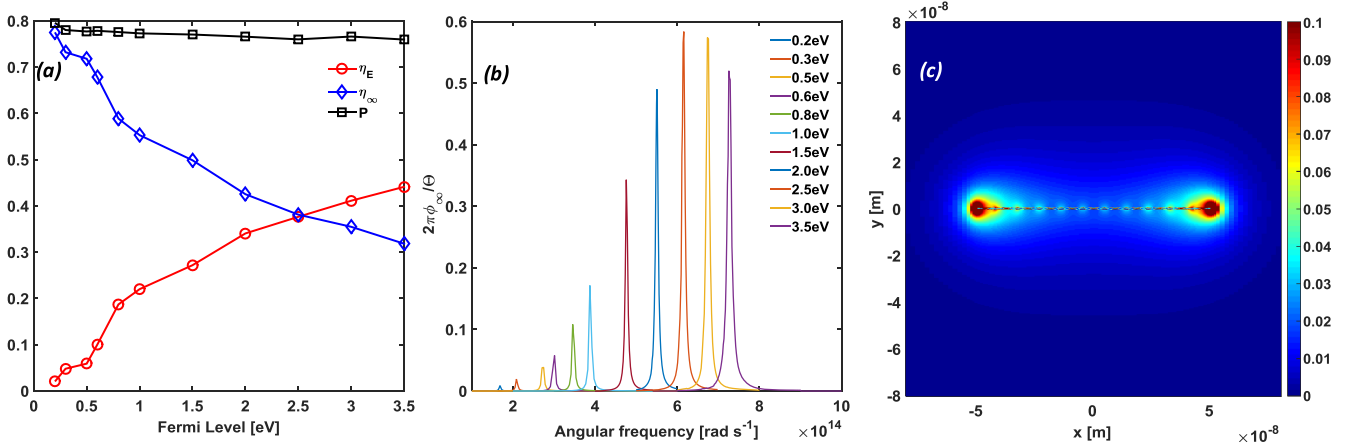


**Figure 5.** (a) Fractional mode losses for different Fermi level. (b) Spectral energy flux of thermal emission calculated from the FSC method implemented by the resistive boundary formulation at different Fermi levels. (c) Normalized real part of the electric field amplitude for the EGSP mode along the ribbon width direction.

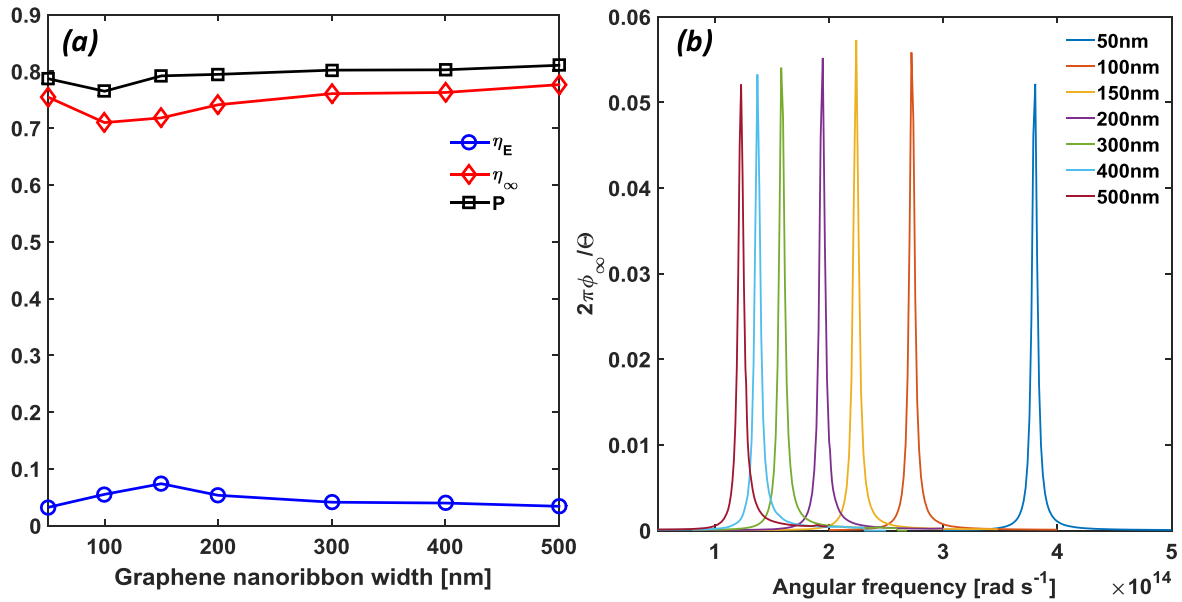


**Figure 6.** (a) Fractional mode losses for different graphene nanoribbon width. (b) Spectral energy flux of thermal emission calculated from the FSC method implemented by the resistive boundary formulation at different graphene nanoribbon width.

separation results in more complex hybridization modes such as the bonding of dipole modes. As for our case, the higher energy symmetric mode and the lower energy anti-symmetric are almost equally pronounced. The normalized real part of electric field amplitudes for the anti-symmetric and symmetric mode are plotted in figures 7(c) and (d) respectively. Here, we only analyze the third symmetric mode based on the QNM mode theory for the near-field thermal emitter, since the anti-symmetric mode could be studied in the same manner, and the third symmetric mode is well isolated from other modes spectrally. Instead of having two fractional mode loss channels in the far-field, thermal emitters in the near-field have three energy loss channels, namely the resistive loss  $\eta_E$  in the emitter, resistive loss  $\eta_A$  in the absorber and the radiative loss  $\eta_\infty$  to the far-field. According to the QNM mode theory in [15], the near-field radiative energy transfer is maximized when the resistive losses in the emitter and the absorber are

balanced as well as the radiative loss to the far-field is minimized. The first condition is naturally satisfied due to the symmetry of the vertically paired graphene nanoribbons along the direction perpendicular to the ribbon plan. In this case, the resistive losses are almost equally distributed into the two ribbons, with one being the emitter and the other being the absorber. To optimize near-field radiative heat flux, we need to change the radiative loss by tuning the Fermi level of the graphene ribbons. Indeed, the radiative loss follows the same trend as it does in the near-field. It is the increase of the Fermi level that results in the lower carrier mobility and larger effective index of the symmetric plasmon mode. As shown in figure 7(a), the blue line represents the radiative loss  $\eta_\infty$  and it monotonically decreases with increasing the Fermi level from 0.2 to 0.8 eV. The red and green lines represent the resistive losses in the absorber and the emitter respectively and they almost coincide with each other throughout the tuning

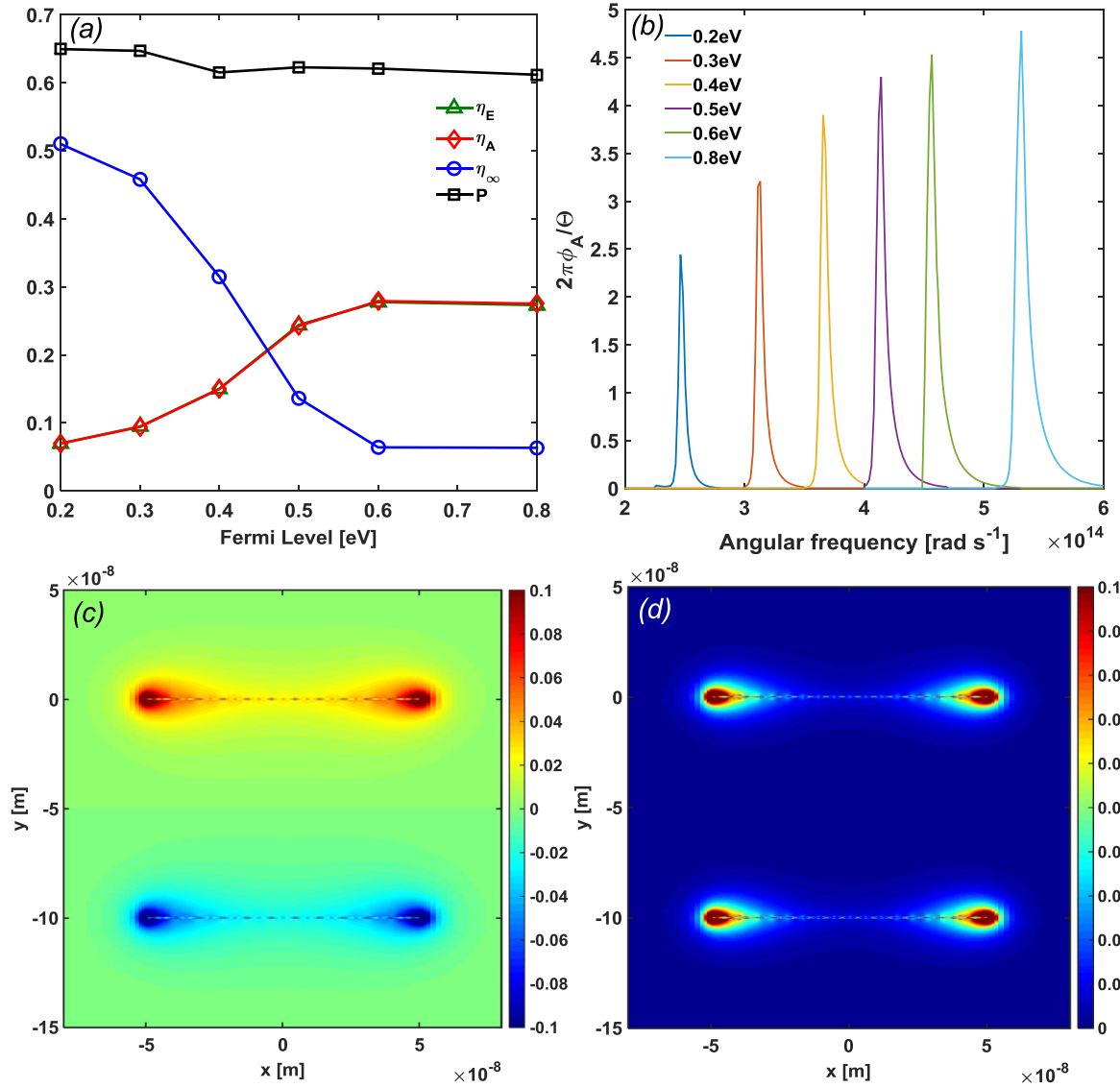


**Figure 7.** (a) Fractional mode losses for different Fermi levels. (b) Near-field spectral energy flux of thermal emission calculated from the FSC method implemented by the resistive boundary formulation at different Fermi levels. Normalized real part of the electric field amplitudes for the (c) anti-symmetric and (d) symmetric modes along the ribbon width direction.

process. As we further increase the Fermi level of paired graphene nanoribbons to 1.0 eV, the resistive and the radiative losses tend to be unchanged, and the reduced near-field radiative heat flux saturates. The non-Hermitian imperfection factor for the paired graphene nanoribbon system is shown as the black line. Figure 7(b) plots the detailed radiative heat flux spectrum at different Fermi levels, where the largest heat flux exceeds the upper limit of far-field radiation by five times. It is expected to render even larger radiative heat flux if the separation is further reduced. It should be pointed out here that the maximized reduced radiative heat flux  $2\pi\phi_A/\Theta$  already exceeds  $P^2$  for the near-field radiative heat transfer between vertically paired graphene nanoribbons. The reason is that there are more than one EGSP mode that are supported at the same resonant frequency, although some of them can be evanescent. This leads to the scenario of degenerate resonant modes where each resonant mode can be optimized. As the graphene nanoribbon pair gets heated up, all such degenerate

modes are excited and the overall reduced radiative heat flux can exceed  $P^2$ . More detailed analysis of those degenerate modes and how to maximize the global radiative heat flux is beyond the scope of this paper. But we can always maximize the contribution to the thermal radiation from a specific mode. If all the modes follow the same trend as we tune the losses, then the global optimization can be achieved.

#### 4. Conclusion

In summary, we demonstrate that the thermal radiation from the 2D graphene nanostructure can be calculated by the FSC method. With the implementation of the resistive boundary formulation, graphene volumetric conductivity is replaced by the surface conductivity when calculating the interaction matrix. By modeling the suspended graphene as resistive boundaries without using the thin film approximation, the

efficiency of the FSC calculation is improved. Furthermore, near- and far-field thermal emission from single graphene nanoribbons and vertically-paired graphene nanoribbons are numerically calculated. Chemical potential proves to play a vital role in tuning the fractional mode losses in the emitter, the absorber or the far-field. In the far-field, the optimization of the thermal emission is achieved by matching the resistive loss in the emitter and the radiative loss to the far-field. In the near-field, it is approached by matching the resistive losses in the emitter and the absorber respectively.

## Acknowledgments

The authors acknowledge funding support from US National Science Foundation (CBET-1253692).

## ORCID iDs

Sheng Shen  <https://orcid.org/0000-0002-4759-2010>

## References

- [1] Freitag M, Chiu H-Y, Steiner M, Perebeinos V and Avouris P 2010 Thermal infrared emission from biased graphene *Nat. Nanotechnol.* **5** 497–501
- [2] Koppens F H L, Chang D E and García de Abajo F J 2011 Graphene plasmonics: a platform for strong light–matter interactions *Nano Lett.* **11** 3370–7
- [3] Luo X, Qiu T, Lu W and Ni Z 2013 Plasmons in graphene: recent progress and applications *Mater. Sci. Eng. R* **74** 351–76
- [4] Chen J et al 2012 Optical nano-imaging of gate-tunable graphene plasmons *Nature* **487** 77
- [5] Jablan M, Buljan H and Soljačić M 2009 Plasmonics in graphene at infrared frequencies *Phys. Rev. B* **80** 1–7
- [6] Mak K F, Sfeir M Y, Wu Y, Lui C H, Misewich J A and Heinz T F 2008 Measurement of the optical conductivity of graphene *Phys. Rev. Lett.* **101** 196405
- [7] Wang F et al 2008 Gate-variable optical transitions in graphene *Science* **320** 206–9
- [8] Giovannetti G, Khomyakov P A, Brocks G, Karpan V M, van den Brink J and Kelly P J 2008 Doping graphene with metal contacts *Phys. Rev. Lett.* **101** 26803
- [9] Wang H, Yang Y and Wang L 2015 Infrared frequency-tunable coherent thermal sources *J. Opt.* **17** 45104
- [10] Zhang Y et al 2015 Independently tunable dual-band perfect absorber based on graphene at mid-infrared frequencies *Sci. Rep.* **5** 18463
- [11] Lin Y-M et al 2011 Wafer-scale graphene integrated circuit *Science* **332** 1294–7
- [12] Liu B, Liu Y and Shen S 2014 Thermal plasmonic interconnects in graphene *Phys. Rev. B* **90** 195411
- [13] Dragoman M and Aldrigo M 2016 Graphene rectenna for efficient energy harvesting at terahertz frequencies *Appl. Phys. Lett.* **109** 113105
- [14] Rodriguez A W, Reid M T H and Johnson S G 2013 Fluctuating-surface-current formulation of radiative heat transfer: theory and applications *Phys. Rev. B* **88** 54305
- [15] Liu B, Li J and Shen S 2017 Resonant thermal infrared emitters in near- and far-fields *ACS Photonics* **4** 1552–7
- [16] Liu B, Gong W, Yu B, Li P and Shen S 2017 Perfect thermal emission by nanoscale transmission line resonators *Nano Lett.* **17** 666–72
- [17] Ahmed I, Khoo E H and Li E 2013 Efficient modeling and simulation of graphene devices with the LOD-FDTD method *IEEE Microw. Wirel. Components Lett.* **23** 306–8
- [18] Wang X-H, Yin W-Y and Chen Z 2015 Broadband modeling surface plasmon polaritons in optically pumped and curved graphene structures with an improved leapfrog ADI-FDTD method *Opt. Commun.* **334** 152–5
- [19] Nayyeri V, Soleimani M and Ramahi O M 2013 Modeling graphene in the finite-difference time-domain method using a surface boundary condition *IEEE Trans. Antennas Propag.* **61** 4176–82
- [20] Nayyeri V, Soleimani M and Ramahi O M 2013 Wideband modeling of graphene using the finite-difference time-domain method *IEEE Trans. Antennas Propag.* **61** 6107–14
- [21] Brar V W, Jang M S, Sherrott M, Lopez J J and Atwater H A 2013 Highly confined tunable mid-infrared plasmonics in graphene nanoresonators *Nano Lett.* **13** 2541–7
- [22] Tamagnone M, Gómez-Díaz J S, Mosig J R and Perruisseau-Carrier J 2012 Reconfigurable terahertz plasmonic antenna concept using a graphene stack *Appl. Phys. Lett.* **101** 214102
- [23] Araneo R, Lovat G and Burghignoli P 2012 Graphene nanostrip lines: dispersion and attenuation analysis *IEEE 16th Workshop on Signal and Power Integrity (SPI)* p 75–8
- [24] Lovat G, Hanson G W, Araneo R and Burghignoli P 2013 Semiclassical spatially dispersive intraband conductivity tensor and quantum capacitance of graphene *Phys. Rev. B* **87** 22
- [25] Shapoval O V, Gomez-Diaz J S, Perruisseau-Carrier J, Mosig J R and Nosich A I 2013 Integral equation analysis of plane wave scattering by coplanar graphene-strip gratings in the THz range *IEEE Trans. Terahertz Sci. Technol.* **3** 666–74
- [26] Burghignoli P, Araneo R, Lovat G and Hanson G 2014 Space-domain method of moments for graphene nanoribbons *8th European Conf. on Antennas and Propagation (EuCAP)* p 666–9
- [27] Gibson W C 2008 *The Method of Moments in electromagnetics* (New York: Chapman and Hall/CRC) p 272
- [28] Rodriguez A W, Reid M T H and Johnson S G 2012 Fluctuating-surface-current formulation of radiative heat transfer for arbitrary geometries *Phys. Rev. B* **86** 220302
- [29] Medgyesi-Mitschang L N, Putnam J M and Gedera M B 1994 Generalized method of moments for three-dimensional penetrable scatterers *J. Opt. Soc. Am. A* **11** 1383
- [30] Tai C-T and IEEE Antennas and Propagation Society, IEEE Microwave Theory and Techniques Society 1994 *Dyadic Green Functions in Electromagnetic Theory* (Piscataway, NJ: IEEE) p 343
- [31] Gao W, Shu J, Qiu C and Xu Q 2012 Excitation of plasmonic waves in graphene by guided-mode resonances *ACS Nano* **6** 7806–13
- [32] Falkovsky L A 2008 Optical properties of graphene *J. Phys.: Conf. Ser.* **129** 12004
- [33] Rytov S M, Kravtsov Y A and Tatarskii V I 1989 *Principles of Statistical Radiophysics 3 Elements of Random Fields* (Berlin: Springer)
- [34] Hwang E H and Das Sarma S 2007 Dielectric function, screening, and plasmons in two-dimensional graphene *Phys. Rev. B* **75** 1–6
- [35] Novoselov K S et al 2005 Two-dimensional gas of massless Dirac fermions in graphene *Nature* **438** 197–200
- [36] Bolotin K I et al 2008 Ultrahigh electron mobility in suspended graphene *Solid State Commun.* **146** 351–5
- [37] Zhao B and Zhang Z M 2016 Enhanced photon tunneling by surface plasmon–phonon polaritons in graphene/hBN heterostructures *J. Heat Transfer* **139** 22701

- [38] Zhao B, Guizal B, Zhang Z M, Fan S and Antezza M 2017 Near-field heat transfer between graphene/hBN multilayers *Phys. Rev. B* **95** 245437
- [39] Nikitin A Y, Guinea F, García-Vidal F J and Martín-Moreno L 2011 Oct Edge and waveguide terahertz surface plasmon modes in graphene microribbons *Phys. Rev. B* **84** 161407
- [40] Nikitin A Y, Guinea F, Garcia-Vidal F J and Martin-Moreno L 2012 Surface plasmon enhanced absorption and suppressed transmission in periodic arrays of graphene ribbons *Phys. Rev. B* **85** 81405
- [41] Aizpurua J, Bryant G W, Richter L J, García De Abajo F J, Kelley B K and Mallouk T 2005 Optical properties of coupled metallic nanorods for field-enhanced spectroscopy *Phys. Rev. B* **71** 1–13
- [42] Sönnichsen C, Franzl T, Wilk T, von Plessen G, Feldmann J, Wilson O and Mulvaney P 2002 Drastic reduction of plasmon damping in gold nanorods **88** 077402
- [43] Joulain K, Mulet J-P, Marquier F, Carminati R and Greffet J-J 2005 Surface electromagnetic waves thermally excited: radiative heat transfer, coherence properties and Casimir forces revisited in the near field *Surf. Sci. Rep.* **57** 59–112
- [44] Christensen J, Manjavacas A, Thongrattanasiri S, Koppens F H L and García De Abajo F J 2012 Graphene plasmon waveguiding and hybridization in individual and paired nanoribbons *ACS Nano* **6** 431–40